Performance Enhancement of the Flexible Transonic Truss-Braced Wing Aircraft Using Variable-Camber Continuous Trailing-Edge Flaps

Robert E. Bartels,[1] and Bret K. Stanford,[2] and Josiah M. Waite[3]
NASA Langley Research Center, Hampton, VA, 23681

Aircraft designers are to a growing extent using vehicle flexibility to optimize performance with objectives such as gust load alleviation and drag minimization. More complex aerodynamically optimized configurations may also require dynamic loads and perhaps eventually flutter suppression. This paper considers an aerodynamically optimized truss-braced wing aircraft designed for a Mach 0.745 cruise. The variable camber continuous trailing edge flap concept with a feedback control system is used to enhance aeroelastic stability. A linearized reduced order aerodynamic model is developed from unsteady Reynolds averaged Navier-Stokes simulations. A static output feedback controller is developed from that model. Closed-loop simulations using the reduced order aerodynamic model show that the controller is effective in stabilizing the vehicle dynamics.

Nomenclature

Variables

A, B, C, D	state matrices
f	frequency
g	structure/rigid body generalized variable
q	dynamic pressure
u	commanded control input
x	state variables
y	state output

Subscripts

a	aerodynamic
C	cruise
D	dive
d	displacement
e	elevator
f	flaps
re	rigid body and structural elastic
r	rate

---

[1] Research Aerospace Engineer, NASA Langley Research Center, MS 340, and AIAA Senior Member.
[2] Research Aerospace Engineer, NASA Langley Research Center, MS 340, and AIAA Associate Fellow.
[3] Research Aerospace Engineer, NASA Langley Research Center, MS 340, and AIAA Member.

1

I. Introduction

Current and future aircraft will make use of aeroelastic design tailoring to optimize performance of a highly flexible wing. While optimized for the designed flight conditions, highly flexible wings can suffer a reduction in performance when off-design. This loss of performance can be counteracted with an active control system, and to a growing extent, modern aircraft use multiobjective flight control to actively enhance aerodynamic performance. For instance, the Boeing 787 uses active wing twist control to optimize the span loading in order to achieve minimum induced drag [1]. Active control is used to alleviate gust and maneuver loading as well as other undesirable effects. The concept of variable camber continuous trailing edge flaps (VCCTEF) for the active control of an aeroelastic wing was originally developed in 2010 and documented in a NASA Innovation Fund study report [2, 3] with the purpose of enhancing aerodynamic performance while reducing drag.

The use of VCCTEF to optimize performance metrics has been extensively studied [1–24]. Many studies have been performed using the generic transport model (GTM). Active control systems utilizing VCCTEF have been developed with the multiple objectives of drag minimization, damping of aeroelastic responses, maneuver and gust load alleviation, to name a few [1, 5, 13, 17, 25]. In several of these studies, load alleviation was performed using VCCTEF for the truss-braced wing aircraft [9, 16]. Chen et al. [16] performed structural optimization and drag minimization using VCCTEF for the truss-braced wing vehicle with an Euler solver coupled with a boundary layer solver. The condition analyzed was at Mach 0.7 and 20,000 ft. That study used an arrangement of trailing edge flaps similar to that used in the current study. Lebofsky et al. [9] used VCCTEF with optimized deflections to minimize the bending moment along the wing. That study used the vortex-lattice method on a rigid wing. There were 10 flaps per side distributed uniformly from root to tip. The condition analyzed was at Mach 0.7.

Since those studies, the NASA funded truss-braced wing aircraft has evolved. Recent phases of the vehicle, being designed by the Boeing Company, targets higher cruise Mach numbers of Mach 0.745 (Phase III) and 0.80 (Phase IV). The configuration analyzed in the current study has been optimized aerodynamically for Mach 0.745. It has not been successfully optimized under a flutter constraint owing to the aerodynamically optimized placement of the strut. One of the objectives of the present study is to assess the capability of a VCCTEF system to control flutter instability. Besides advancing the VCCTEF concept for the transonic truss-braced wing vehicle, this objective touches upon the NASA Advanced Air Transport Technology projects addressing active structural control for continuous distributed control surfaces. Another objective is to assess an unsteady Reynolds averaged Navier-Stokes (URANS) based aerodynamic reduced order model for a complex configuration such as the truss-braced wing. The accuracy and range of applicability of that model will be assessed as well as the performance of a feedback controller based on that model.

This paper will present flutter suppression results for the Mach 0.745 transonic truss-braced wing vehicle. The vehicle configuration is shown in Figure 1. The unsteady computational fluid dynamics and its reduced order model will be discussed. The development of the feedback controller will be discussed followed by an assessment of the open and closed-loop performance of the Mach 0.745 transonic truss-braced wing vehicle.

II. Structural Model

The structural model for the Mach 0.745 transonic truss-braced wing (TTBW) aircraft was developed by the Boeing Company under a NASA Phase III NRA contract. The finite element model used in the present work is shown in Figure 2. The model has 125,230 grid points, 129,280 shell elements, and 11,588 beam and bar elements. The fuselage center section and wing structure comprise most of the elements. The aft fuselage is modeled as a rigid beam, and the tail assemblage as flexible beams. As received, the model had only nominal uniform element thicknesses sufficient to satisfy static load requirements. While the vehicle shape has been aerodynamically optimized for its target Mach number, it has not been weight optimized under a flutter constraint. Furthermore, because the strut/wing placement is primarily due to aerodynamic considerations, the Phase III Mach 0.745 TTBW structural model does not

**Fig. 1 Mach 0.745 transonic truss-braced wing aircraft.**

satisfy a flutter constraint for any reasonable weight distribution.

One of the objectives of the present work is to ascertain whether it is possible to stabilize the structure with a feedback control system. In the present work the structure has been optimized for static load cases (linear only) at operational empty weight (OEW) and full payload/fuel weight distributions, for a 2.5 g pull-up and a -1 g push-over maneuver at 40k ft, Mach 0.745 (cruise) flight conditions. Over 10,000 skin, composite ply and beam thickness properties were separately optimized to minimize weight. The result is that apart from several critical areas, many wing skin thicknesses have been reduced substantially and overall weight reduced by 1-2 percent.

Because of the unusual load path of the truss-braced structure, static loading can and likely will alter the aeroelastic behavior of the vehicle by geometrically stiffening the wing and strut. Previous papers have addressed the effect of structural stiffening on flutter onset [26, 27]. This paper does not address that effect. Normal modes analysis about the unloaded optimized structure at the full payload/fuel weight is performed. Nastran doublet-lattice and URANS CFD analyses have shown that both symmetric and antisymmetric modes are active in inducing flutter onset. Never-the-less, to limit the computational burden of creating a URANS-based reduced order model, only symmetric modes are used in the following analyses. This inevitably alters the flutter mechanism, but is a necessary expedient. Figure 3 shows the 1st symmetric bending mode – one of the least damped modes in the present analyses. Additional modes are shown in Figures 4 and 5. Table 1 provides modal frequencies of the optimized model along with mode descriptions. The structural model includes flaps and it will be noted that the last two modes are mainly due to flap flexibility. Flap modes for commanded control will be defined in a subsequent section which do not have flexibility associated with them.

III.   Computational Fluid Dynamics Model

Owing to its ability to combine high-fidelity computational fluid dynamics (CFD) with a flexible structure, the FUN3D v13.1 code is used in the present study. The Navier-Stokes code FUN3D (fully unstructured three-dimensional Navier-Stokes) is a finite volume unstructured CFD code for compressible flows [28, 29]. FUN3D solves the steady and unsteady Reynolds-averaged Navier-Stokes (URANS) flow equations loosely coupled with the Spalart-Allmaras turbulence model [30] on a tetrahedral mesh. The most commonly used method of modeling the structure, and that
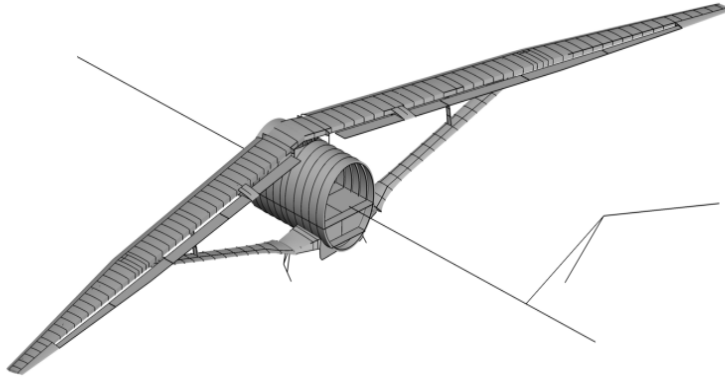
Fig. 2 Finite element structural model.

Table 1 Frequencies and descriptions of symmetric modes for optimized structure.

mode number	frequency (Hz)	pulse Δz_{max} (in)	description
1	~ 0.0	0.3*	pitch
2	~ 0.0	0.02	plunge
3	1.40	0.02	1st wing/body bending
4	1.72	0.06	1st wing bending
5	2.29	0.06	1st wing torsion/ outboard wing bending
6	2.82	0.06	2nd wing bending
7	3.25	0.05	2nd wing torsion/ outboard wing bending
8	4.62	0.06	3rd wing bending
9	6.34	0.18	4th wing bending
10	9.31	0.04	3rd wing torsion
11	10.3	0.04	4th wing torsion
12	10.7	0.06	5th wing torsion
13	11.5	0.18	6th wing torsion
14	12.9	0.04	7th wing torsion
15	14.5	0.13	1st strut bending
16	15.9	0.18	5th wing bending/ 2nd strut bending
17	18.0	0.10	1st inboard/mid flap bending
18	18.85	0.25	2nd mid flap bending

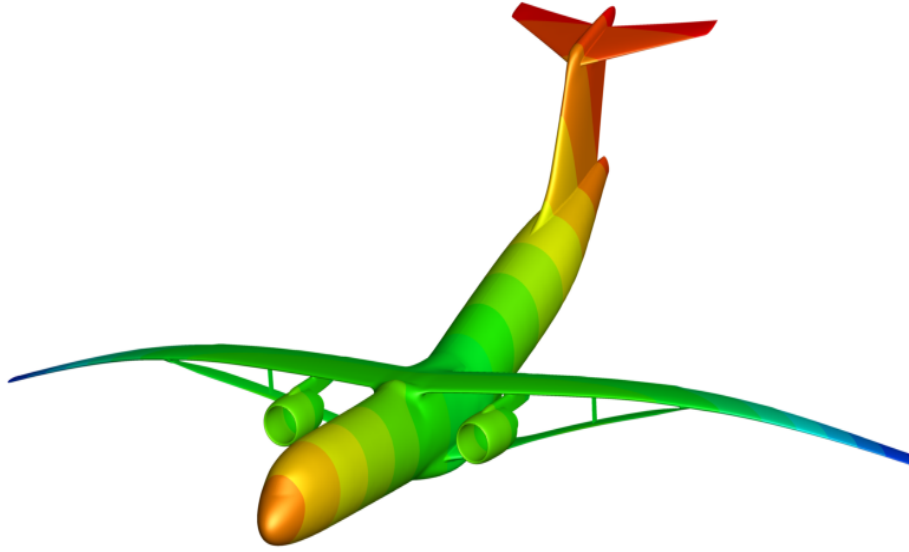* Approximately 0.01 degree

Fig. 3 1st symmetric wing/body bending mode.

Fig. 4 1st symmetric wing bending mode.

**Fig. 5** 2nd **symmetric wing bending mode.**

used here, is by linear normal modes. The control surfaces are modeled as modes that can be actuated in a URANS-based reduced order model incorporating a feedback control loop.

The CFD mesh has 35 million nodes. The vehicle and CFD mesh used in the present analysis are in the 1 g cruise shape. Solutions are obtained at a nominal angle of attack of 2 degrees in order to approximate a 1 g loading condition. Since the aircraft is already deflected based on 1 g loading, the static aerodynamic load at that angle of attack is removed from the equations of structural dynamics in order to maintain the 1 g wing shape apart from other external disturbances. All deflections presented here are a difference from that reference shape.

The VCCTEF concept of control surface segments connected by elastomer membrane is implemented in this study by creating 18 control surfaces. The layout of the VCCTEF concept is shown in Figure 6. In this study, the flaps are created by dividing the finite element model flaps into two to four additional segments each. There are four inboard flaps and fourteen outboard flaps. Since the current study includes the engine nacelle/pylon structure, the 4th and 5th flaps have a gap between them for supporting structure. There is also a slight gap between the 7th and 8th flaps where the jury strut connects to the wing. Each control surface consists of three chordwise segments that deflect in a 1, 2 and 6 degree parabolic arc schedule. The spanwise distribution of deflections follow Bernstein polynomials. This is motivated by the need for a smooth variation in deflections between adjacent flaps in order to accommodate elastomer material. Six Bernstein polynomials, which are shown in Figure 8, will be used for the inboard and six polynomials for the outboard flap sets.

From the CFD meshing stand point, in order to maintain a smooth and physically realistic transition between each segment, the surface mesh is clustered along control surface discontinuities (spanwise and leading/trailing edges), as shown in Figure 7. Table 2 indicates the mode assignment and the polynomial order of the inboard and outboard flaps. Since these modes are for commanded control surface deflections, they do not include actuator flexibility. Figures 9 and 10 illustrate deflections for several polynomial shapes. The final control surface mode indicated in Table 2 is the horizontal stabilator shown in Figure 11.

The flight condition is Mach 0.745 at 40,000 ft, AoA = 2 degrees. All system identification and dynamic solutions are initiated after a steady state solution at this flight condition. For flutter analyses, dynamic pressure at cruise and

6
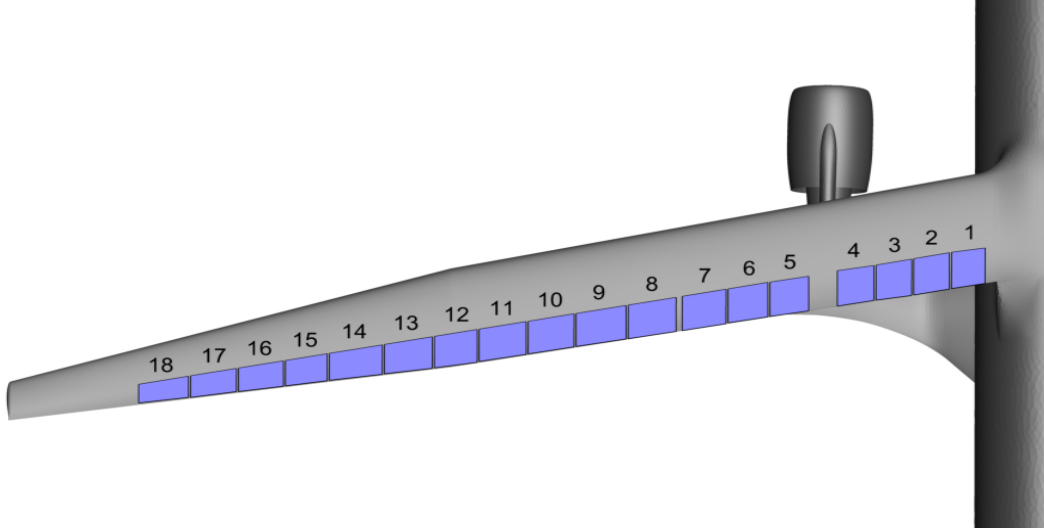
Fig. 6 VCCTEF layout.

Table 2 Control surface shape function/mode definitions.

mode assignment	n	pulse δ (deg)	flap set
19	0	0.30	inboard
20	1	0.10	inboard
21	2	0.10	inboard
22	3	0.10	inboard
23	4	0.10	inboard
24	5	0.30	inboard
25	0	0.30	outboard
26	1	0.12	outboard
27	2	0.10	outboard
28	3	0.10	outboard
29	4	0.12	outboard
30	5	0.30	outboard
31	rotation	0.1	horizontal tail

dive speed is obtained by varying density at constant Mach number and speed. This does not result in matched flutter solutions, but does allow the use of a single aerodynamic reduced order model for all flutter simulations.

IV.   Vehicle Dynamics

Developing a control system for the truss-braced wing aircraft requires a linearized state-space model of the structure and aerodynamics. The linearized plant dynamics can be written

$$\dot{x} = Ax + Bu \tag{1}$$

$$y = \left\{ \begin{array}{c} y_{re} \\ y_a \end{array} \right\} = \left[\begin{array}{cc} C_{re} & 0 \\ 0 & C_a \end{array} \right] \left\{ \begin{array}{c} \xi_{re} \\ \xi_a \end{array} \right\} \tag{2}$$
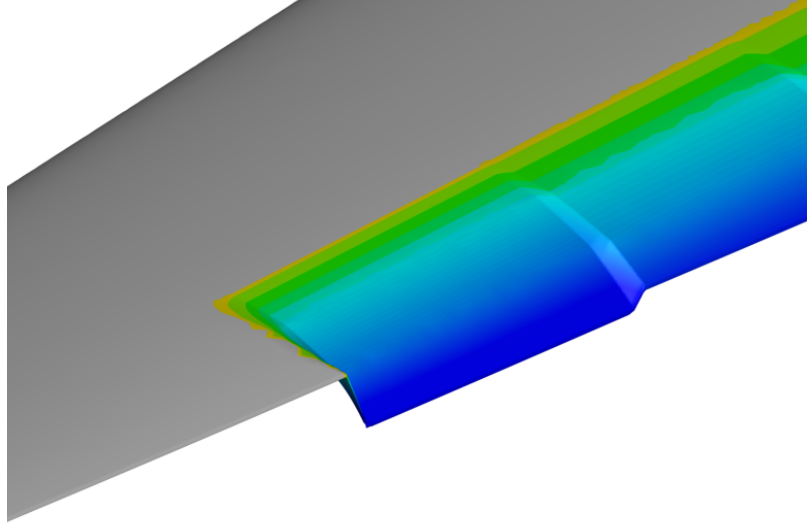
(a) Flap deflection
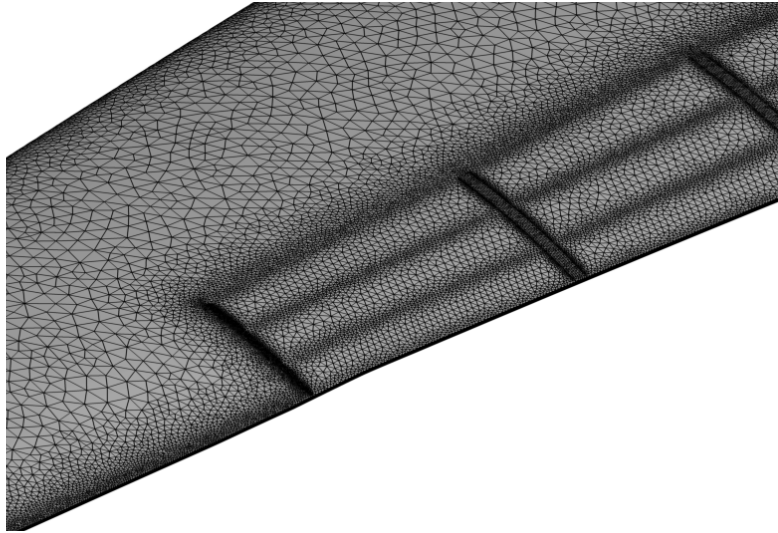
(b) Surface mesh

Fig. 7 Parabolic arc flap deflections.

where $\xi_a = \{x_a \quad \dot{x}_a\}^T$, $\xi_{re} = \{x_{re} \quad \dot{x}_{re}\}^T$. ξ_{re} are the rigid body and flexible states and ξ_a are the augmented aerodynamic lag states. The complete state variable array is
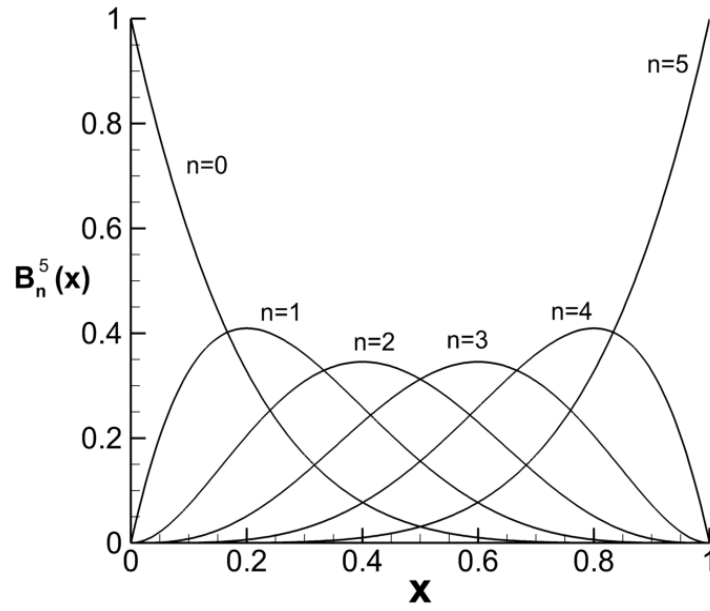
$$x = \begin{bmatrix} \xi_{re} \\ \xi_a \end{bmatrix} \quad . \tag{3}$$

The measured outputs y are displacements and rates at a set of sensor locations. The flexible and rigid body outputs are defined by

$$C_{re} = \begin{bmatrix} C_d & 0 \\ 0 & C_r \end{bmatrix} \tag{4}$$

where $C_d = I$ outputs modal displacements and $C_r = I$ outputs modal rates. The commanded control surface inputs $u = \{u_f \quad u_e\}^T$ include flaps and elevator.
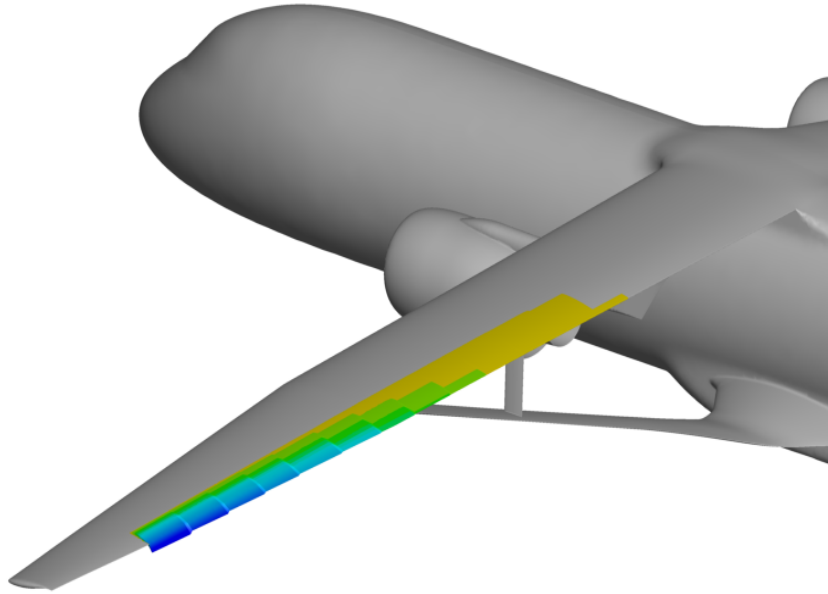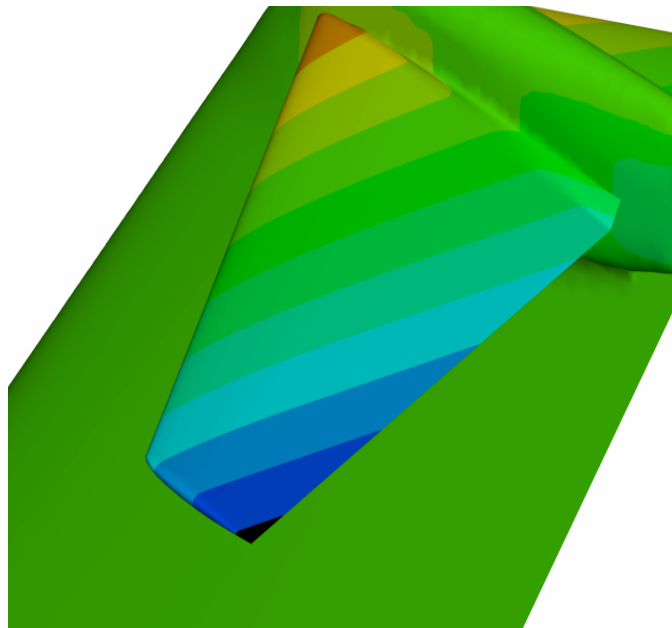
8

Fig. 8 Bernstein polynomials $B_n^5(x)$.
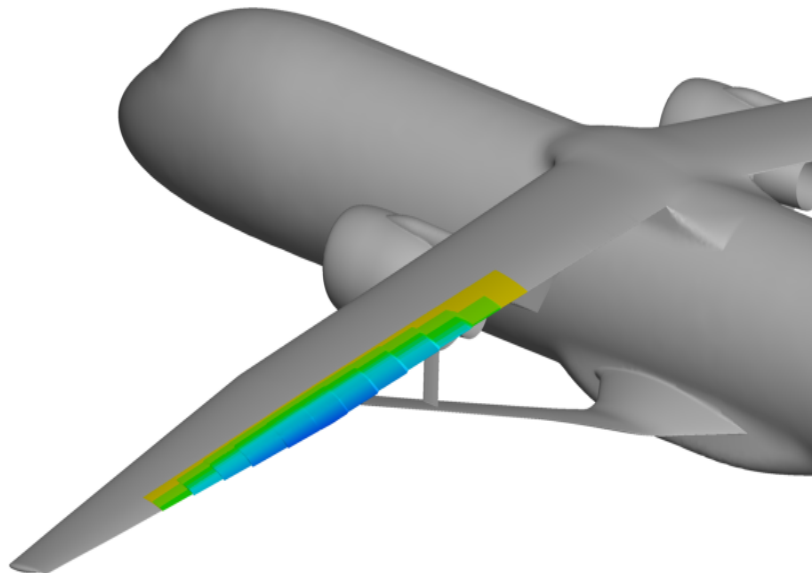
Fig. 9 Typical flap deflections for static drag reduction using $B_3^5(x)$ distribution.

Fig. 10 Typical flap deflections for flutter suppression using $B_5^5(x)$ distribution.

Fig. 11 Horizontal stabilizer/elevator.

The combined state matrices are

$$A = \begin{bmatrix} A_{re} + q_\infty B_{re} D_a G_s & q_\infty B_{re} C_a \\ B_a G_s & A_a \end{bmatrix} \quad , \quad B = \begin{bmatrix} q_\infty B_{re} D_a G_c \\ B_a G_c \end{bmatrix}$$

$$G_s = \begin{bmatrix} C_{re} \\ 0 \end{bmatrix} \quad , \quad G_c = \begin{bmatrix} 0 \\ I \end{bmatrix} \quad ,$$

(5)

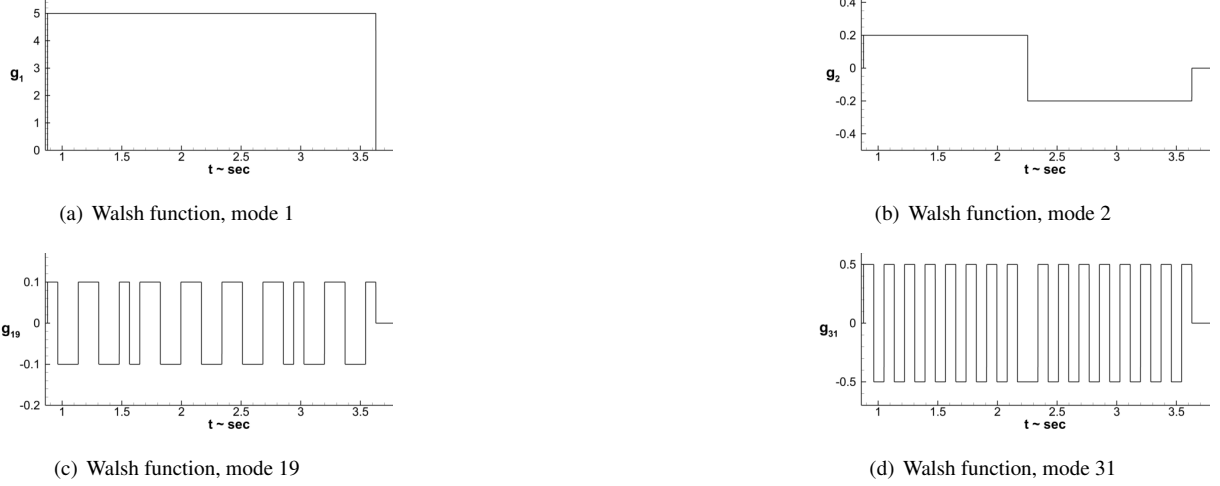which include both the structural/rigid body and aerodynamic systems. The dynamic pressure is q_∞, and the aerodynamic state matrices are A_a, B_a, C_a, D_a. The state matrices of the structural dynamics and rigid body degrees of freedom are A_{re}, B_{re}, C_{re}, D_{re}. The following section outlines how the aerodynamic matrices are obtained.

A. Reduced Order Aerodynamic Model

The continuous aerodynamic state matrices A_a, B_a, C_a and D_a are derived from discrete state matrices created using the AEROM software [31]. In the URANS system excitation using the FUN3D code, the thirty one modes are simultaneously excited with Walsh function pulses. Examples of Walsh function pulses with different excitation levels for each mode are shown in Figure 12. The maximum mode deflections in inches of each mode in the system identification are indicated by column 3 of Table 1. The magnitudes of angular pulse deflections of the control surfaces are indicated in Table 2. These magnitudes of motion in the system identification step were limited either by the CFD mesh deformation scheme or by the smoothness and robustness of the interpolation of structural node displacements to CFD nodes. Pulse magnitudes much larger than these values resulted in code failure due to negative volumes. For this reason, the scope of this model has to be considered somewhat limited beyond its use for a demonstration of flutter suppression.

The PULSE algorithm is used to extract individual output responses from simultaneous inputs and output responses. The ERA Eigensystem Realization Algorithm (ERA) [32] /System Observer Controller Identification Toolbox (SOCIT) and the Observer Kalman Identification (OKID) [33] algorithms are used to create the discrete-time state-space model of the aeroelastic system. These algorithms use the Markov parameters (discrete-time impulse responses) of the systems of interest to perform the required state-space realization. The individual responses are then processed via the ERA in order to generate the state-space aerodynamic model.

The TTBW aircraft is complex aerodynamically and for that reason care was taken to create a good quality aerodynamic reduced order model. The time step size of the aerodynamic system identification is set by requiring 40 time steps over which a fluid particle moved across the mean aerodynamic chord length and 6-10 time steps over which a fluid particle moved across the trailing edge flaps. Requiring 4 seconds of total time to adequately excite the lowest structural modes results in nearly 36,000 time steps. The solution was monitored over its extent to ensure overall subiterative convergence at each time step. The root mean square and max/min values of lift coefficient and moment coefficient normalized to the final value at each time step is shown in Figure 13. Seven subiterations were used. As can be seen in those figures, at 5-6 subiterations even the slowest converging time steps were 99.9 percent converged in lift coefficient and 99.8 percent converged in moment coefficient. A comparison of the CFD modal response and the response due to the ROM are shown in Figure 14. While the two solutions are not identical, the responses are generally close.

11

(a) Walsh function, mode 1

(b) Walsh function, mode 2

(c) Walsh function, mode 19

(d) Walsh function, mode 31

Fig. 12 Representative Walsh function modal pulses.

(a) C_L

(b) C_{My}
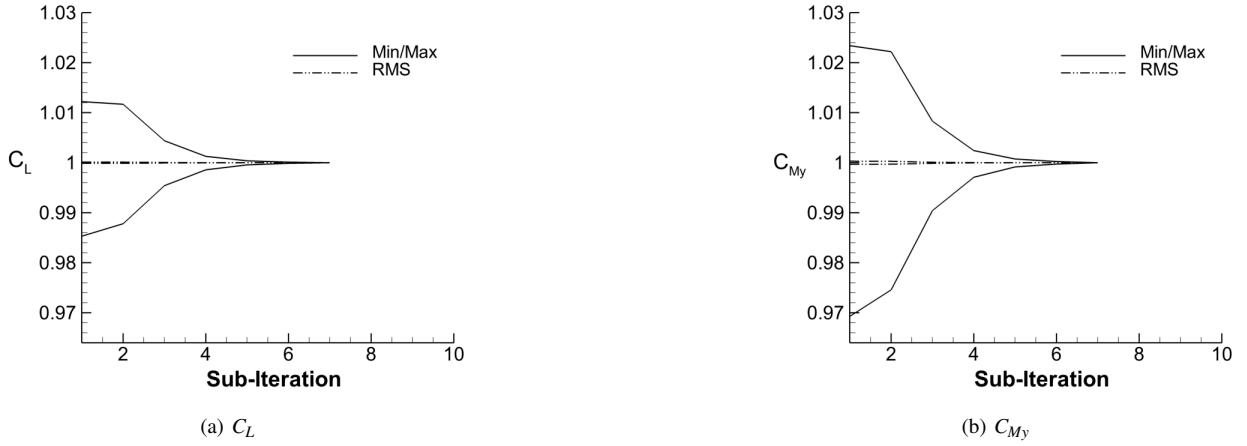
Fig. 13 Cumulative lift and moment coefficient iterative convergence.

B. Control Objective and Gain

The optimal feedback matrix is computed using static output feedback (SOF), as discussed in Ref. [34]. Rate sensor feedback from 18 locations on the vehicle drives control surfaces. The 18 locations are shown in Figures 15. These locations are chosen to provide observability to all 18 flexible modes. Because the following simulations are performed exclusively in state-space, it is necessary to obtain the measured sensor rates from the state variable x. The measured sensor rates are obtained by the transformation $\Delta\dot{z} = TC_r\dot{x}_{re}$ where T converts the 18 rigid body and flexible rates in state-space to measurable rates at the sensor locations. The control law then takes the form

$$u = -K\Delta\dot{z} = -KTC_r\dot{x}_{re} \quad . \tag{6}$$

K is the gain matrix and $\Delta\dot{z}$ are the measured displacement rates at the 18 sensor locations. The performance index then becomes

$$J = \frac{1}{2}\int_0^\infty (\dot{x}_{re}^T C_r^T T^T QTC_r\dot{x}_{re} + u^T Ru)dt \quad . \tag{7}$$

The matrix Q more heavily weights the lowest frequency modes. The matrix R is set to minimize the flap and elevator settings. In minimizing the performance index for suppressing flutter, all the control surfaces, including the horizontal
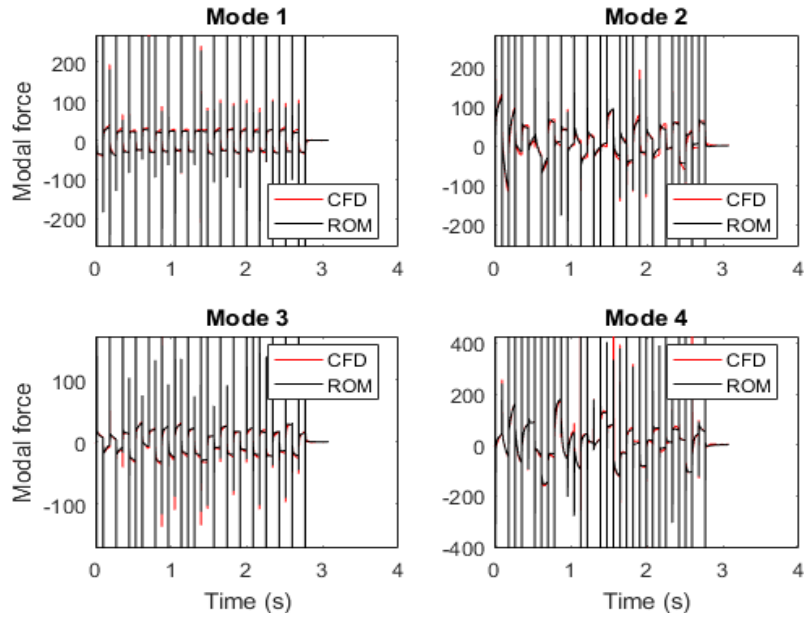
Fig. 14 Comparison of ROM and CFD Walsh pulse excitation responses.

(a) Upper wing, body and tail
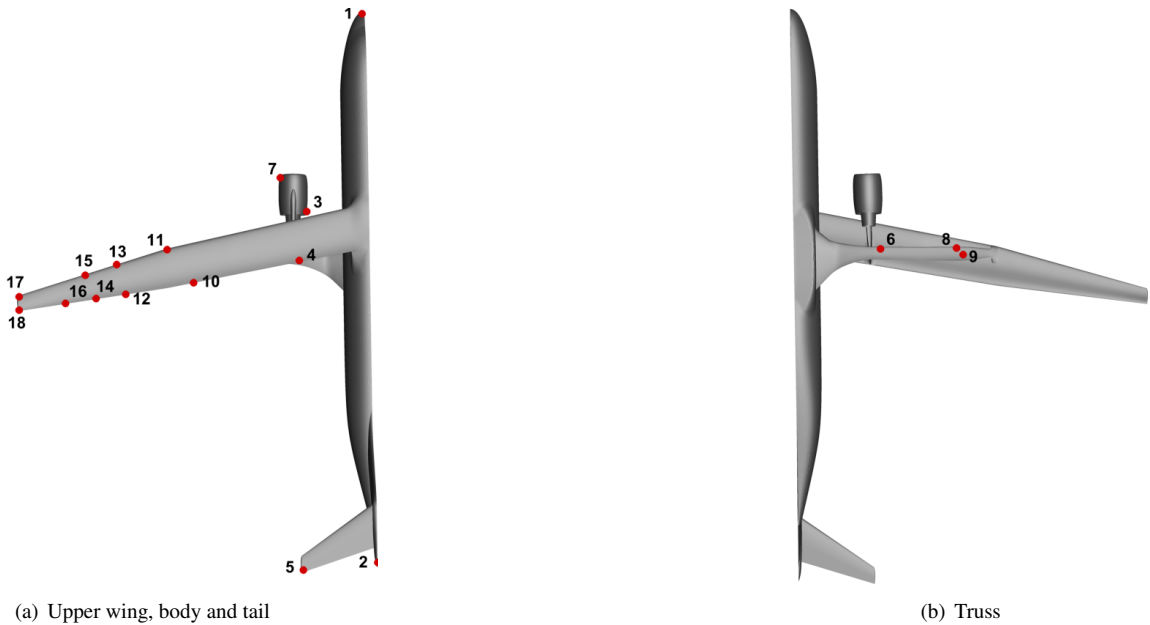
(b) Truss

Fig. 15 Vehicle sensor locations.

tail, are active. This will be clearly seen in subsequent results.
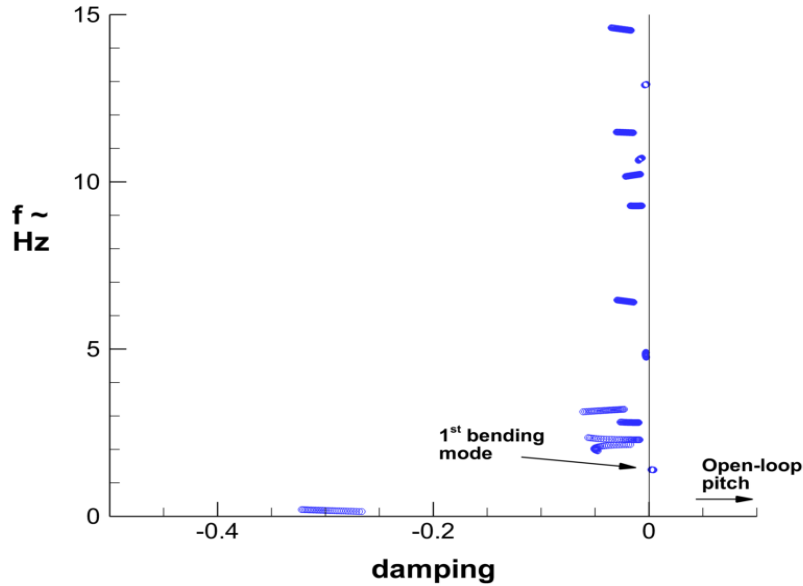
V.   Results

A.   Open-loop Behavior

The objective of this work is to enhance the aeroelastic performance of the TTBW using active control surfaces including an all movable horizontal tail to stabilize pitch and plunge. To first assess flutter characteristics of the

Table 3 Nastran 1st symmetric bending instability onset.

frequency (Hz)	q/q_C (psi)
1.47	0.74

Fig. 16 Open-loop poles due to ROM, no structural damping, $q_C \rightarrow 1.15 q_D$.

vehicle, MSC.Nastran flutter analysis has been performed using symmetric modes, including pitch and plunge, and doublet-lattice aerodynamics. The resulting dynamic pressure at onset of flutter involving the 1st wing/body symmetric bending mode is shown in Table 3. This instability is at approximately 1.47 Hz and occurs well below cruise speed. An eigenanalysis of the URANS-based ROM that includes aircraft pitch and plunge indicates that, in addition to an instability of the pitch and plunge modes, there is a very slight instability of the 1st wing/body bending at approximately 1.4 Hz. Although not shown here, this instability occurs at all nonzero dynamic pressures. Figure 16 shows the ROM open-loop poles for dynamic pressures from cruise to 15 percent beyond dive speed. The URANS-based ROM is very slightly undamped in the 1st wing/body bending at all non-zero dynamic pressures and 0.2 percent undamped at cruise speed dynamic pressure, q_C. At dive speed dynamic pressure, q_D, the 1st wing/body bending is 0.4 percent undamped. All other modes are at least slightly damped.

Figure 17 compares a URANS 1st wing/body bending time history with that due to the URANS ROM at q_C. In these simulations the aircraft pitch and plunge modes and all control surface deflections are set to zero. The time histories over seven oscillations indicates that the ROM is performing well at predicting the slight undamping of that mode. Figure 18 presents damping ratio versus frequency at q_D from the URANS time marching and ROM eigenvalue analysis. ROM damping ratio is computed from the eigenvalues while the URANS damping ratio is calculated using the log-decrement method. The damping and frequency of the 1st wing/body bending match quite well as well as that of the inboard torsion/outboard wing bending mode at 2.29 Hz. Note that several modes in the vicinity of $3.7 - 3.9$ Hz have become slightly unstable at this dynamic pressure. These appear to be the nacelle/outboard wing bending and several torsion modes (modes 6-8 in Table 1).
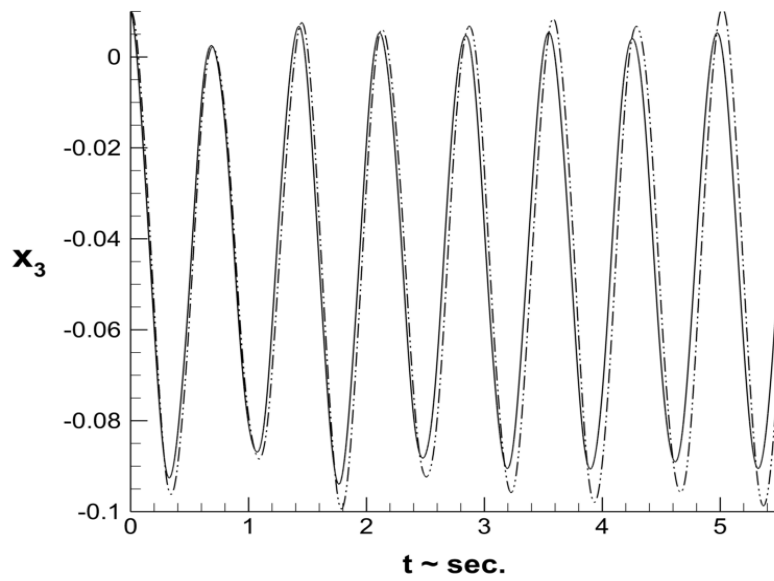
Fig. 17 Time history of 1st symmetric bending generalized variable at q_C, no structural damping ($-$ URANS, $- \cdot \cdot$ ROM).
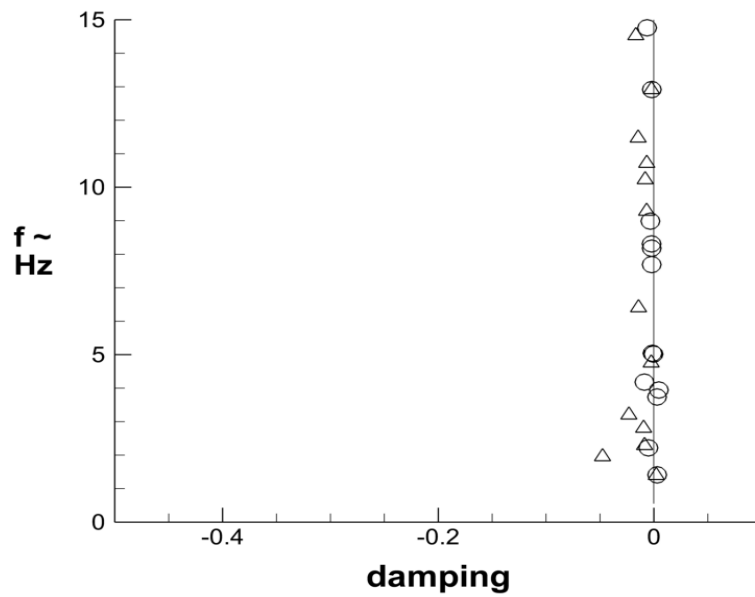

Fig. 18 Open-loop damping versus frequency at q_D, no structural damping ($\bigcirc$ URANS, $\triangle$ ROM).

B. Feedback Control Development and Closed-loop Performance

In a real aircraft, it is expected that higher frequency modes will experience higher structural damping. With that fact in view, the lightly damped higher frequency poles in the present case will most likely not be a concern. The slightly undamped 1st wing/body bending mode and strongly unstable rigid body pitch and plunge modes require control. The first eight modes are accordingly given the highest weighting in the Q matrix. Figure 19 presents the resulting open and closed-loop poles. The most critical modes below 6 Hz are strongly damped by the control system. The resulting gain matrix provides roughly five percent additional damping to the 1st wing/body bending mode. The pitch and plunge modes are very strongly damped. Above 6 Hz there is very little difference between open and closed-loop behavior, which as noted above, is not considered to be an issue.

To test the functionality of the controller in the time domain, a Simulink model has been constructed. The state-space model simulated here is

$$\dot{x} = (A - BK\tilde{C})x$$

$$y_{re} = \begin{bmatrix} C_d & 0 \\ 0 & C_r \end{bmatrix} \begin{Bmatrix} x_{re} \\ \dot{x}_{re} \end{Bmatrix} \quad , \quad \Delta z = TC_d x_{re} \tag{8}$$

where $\tilde{C} = \begin{bmatrix} 0 & TC_r & 0 \end{bmatrix}$. Several tests have been performed using initial modal velocities and displacements for conditions at q_C and $1.15q_D$. The results of Figure 20 are time histories of the average deflection at sensor 17 and 18 and the tip twist due to an initial displacement of modes 3-18, while Figure 21 shows the control surface deflections required to control the vehicle. Rigid body degrees of freedom are free but not excited externally. Note that this simulation includes two percent structural damping on flexible modes below 10 Hz and five percent structural damping on modes above 10 Hz. Most of the initial displacement is damped out within 1 second, while the critical flutter mode is fully damped within 3-4 seconds. Time histories of the deflection of several inboard and outboard flaps, and the horizontal tail required to control the vehicle flexibility, are shown in Figure 21. As expected, the outboard flaps are the most active in suppressing the flutter. It is not entirely surprising that the horizontal stabilizer is also active in suppressing the flexible modes since the 1st wing/body bending mode includes considerable tail motion (see Figure 3).

A notable feature of this simulation is the rather large displacement of the outboard flaps for the wing tip deflections. Simulations with initial modal velocity that resulted in wing tip deflections of $1 - 2$ inches resulted in even larger flap deflections. When the magnitudes of the excitations of the vehicle pitch and plunge modes are sufficient to result in several inches of nose and tail deflection, the control surface deflections become unreasonably large.

VI. Concluding Remarks

This paper has investigated the ability of variable camber continuous trailing edge flaps to suppress unwanted aeroelastic interactions in the flexible transonic truss-braced wing vehicle. The version of the aircraft used here has been optimized aerodynamically, but has not been configured to preclude a slight flutter instability at cruise dynamic pressure. For that reason, one of the functions of the variable camber continuous trailing edge flaps is to suppress flutter. To develop the control system necessary to suppress flutter, an unsteady Reynolds averaged Navier-Stokes based reduced order aerodynamic model has been developed. The coupled aerodynamic and structural reduced order models have been used to develop a sensor rate feedback control system that utilizes eighteen distributed wing trailing edge flaps and a horizontal tail to control the flexible vehicle. Rate feedback at eighteen locations on the vehicle are used to drive the controller. The controller coupled with a VCCTEF layout with parabolic arc deflection scheduling and Bernstein polynomial spanwise distribution deflections has been found to be effective in suppressing flutter as well as aeroelastically shaping the wing using distributed continuous camber trailing edge flaps.

There are many issues that still need to be addressed. Note that while simultaneous input/output is more efficient than separate modal excitation, the resulting build up of surface displacements due to simultaneous motion (and
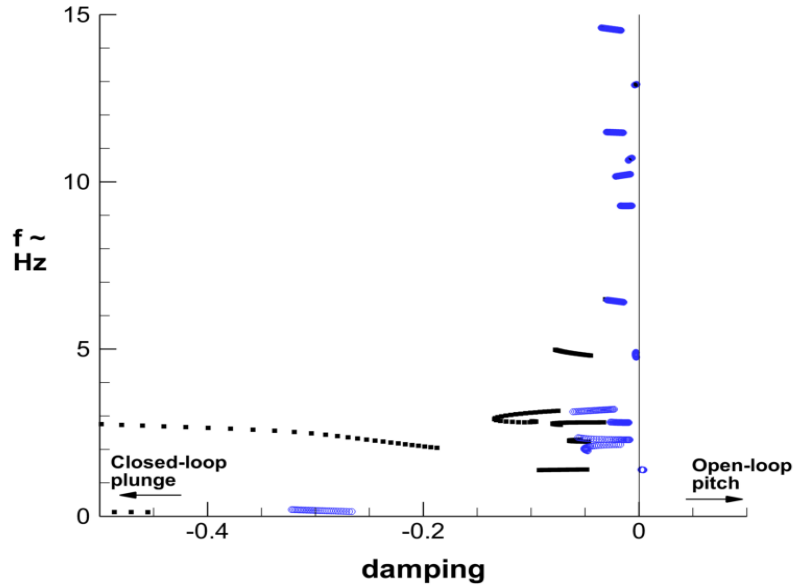
Fig. 19 Open and Closed-loop poles due to ROM, no structural damping (blue circles open-loop, ·· closed-loop), $q_C \rightarrow 1.15 q_D$**.**

consequent breakdown of mesh motion) limited significantly the extent of travel for any one of the modes. The pitch mode pulse was especially limited because of the size of vehicle nose and tail displacements for even small pitch angles. Thus, the range of applicability of the present model, and the method of system identification are issues that will need to be further addressed. It may be necessary to excite modes individually to reach realistic amplitudes for all the modes. Other pulse shapes may allow larger amplitudes and at the same time enable robust mesh deformation.

The open-loop reduced order aerodynamic model has been validated against full URANS simulations for moderate deflections of the flexible modes. Verification of rigid body modes and the closed-loop performance of the model against URANS simulations have yet to be done. It appears possible to command a static deflection of control surfaces, such as might be required to optimize drag using flexible wing shaping. Targeting a realistic flexible vehicle shape for drag minimization will require a robust system identification with much larger pulse sizes. Future enhancements would be to include lift, drag and moment coefficients as aerodynamic degrees of freedom in the reduced order aerodynamic model. This would allow trimming the vehicle and including drag minimization as part of the control system objective function.
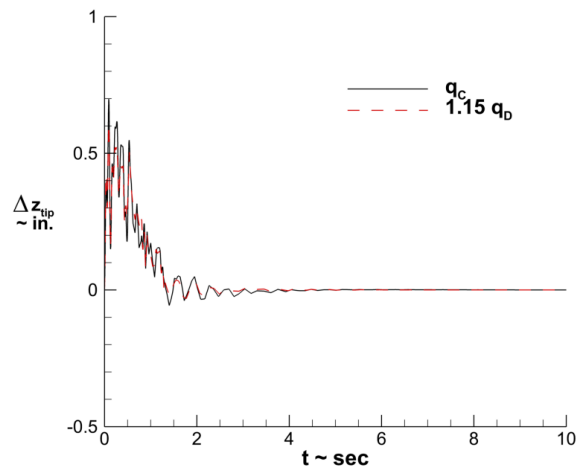
(a) Average tip deflection
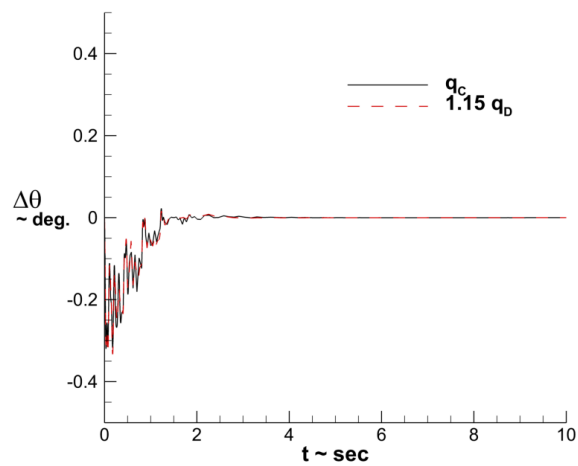
(b) Tip twist

Fig. 20 Vehicle state versus time, closed-loop with initial modal deflection.

References

[1] Nguyen, N. and Tal, E., "A Multi-Objective Flight Control Approach for Performance Adaptive Aeroelastic Wing," *AIAA SciTech Forum*, No. 2015-1843, Kissimmee, FL, January 2015.

[2] Nguyen, N., "Elastically Shaped Future Air Vehicle Concept," Nasa innovation fund aware report, NASA Innovative Partnerships Program, 2010.

[3] Nguyen, N. and Urnes, J., "Aeroelastic Modeling of Elastically Shaped Aircraft Concept via Wing Shaping Control for Drag Reduction," *AIAA Atmospheric Flight Mechanics Conference*, No. 2012-4642, August 2012.

[4] Kaul, U. K. and Nguyen, N. T., "Drag Optimization Study of Variable Camber Continuous Trailing Edge Flap (VCCTEF) Using Overflow," *AIAA Aviation Forum*, No. 2014-2444, Atlanta, GA, June 2014.

[5] Lebofsky, S., Ting, E., and Nguyen, N. T., "Aeroelastic Modeling and Drag Optimization of Aircraft Wing with Variable
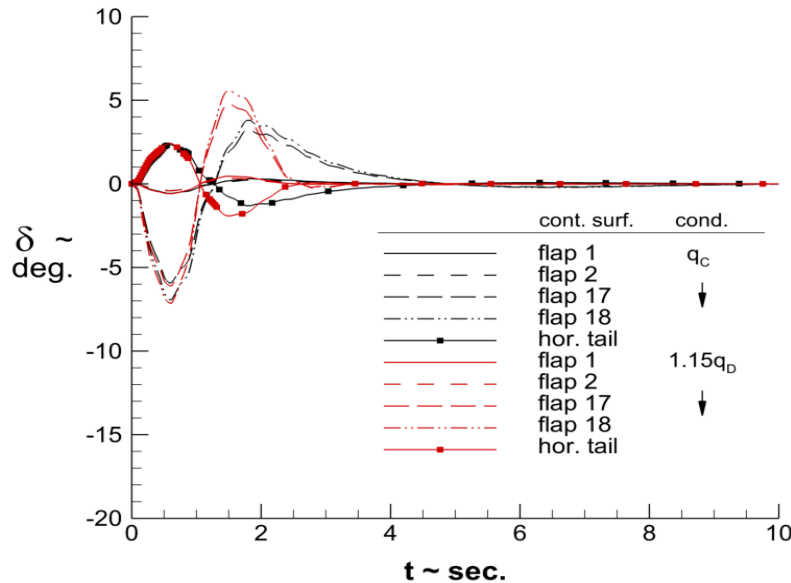
Fig. 21 Control surface deflections, closed-loop with initial modal deflection.

Camber Continuous Trailing Edge Flap," *AIAA Aviation Forum*, No. 2014-2443, Atlanta, GA, 2014.

[6] Swei, S. S.-M. and Nguyen, N., "Aeroelastic Wing Shaping Control Subject to Actuation Constraints," *AIAA SciTech Forum*, No. 2014-1041, National Harbor, Maryland, January 2014.

[7] Kaul, U. K. and Nguyen, N. T., "A 3-D Computational Study of a Variable Camber Continuous Trailing Edge Flap (VCCTEF) Spanwise Segment," *AIAA Aviation Forum*, No. 2015-2422, Dallas, TX, June 2015.

[8] Lebofsky, S., Ting, E., and Nguyen, N. T., "Multidisciplinary Drag Optimization of Reduced Stiffness flexible Wing Aircraft With Variable Camber Continuous Trailing Edge Flap," *AIAA SciTech Forum*, No. 2015-1408, Kissimmee, FL, January 2015.

[9] Lebofsky, S., Ting, E., Nguyen, N., and Trinh, K., "Optimization for Load Alleviation of Truss-Braced Wing Aircraft With Variable Camber Continuous Trailing Edge Flap," *AIAA Aviation Forum*, No. 2015-2723, Dallas, TX, June 2015.

[10] Nguyen, N. T., Ting, E., and Lebofsky, S., "Aeroelastic Analysis of a Flexible Wing Wind Tunnel Model with Variable Camber Continuous Trailing Edge Flap Design," *AIAA SciTech Forum*, No. 2015-1405, Kissimmee, FL, January 2015.

[11] Precup, N. Mor, M. and Livne, E., "The Design, Construction, and Tests of a Concept Aeroelastic Wind Design Model of a High-Lift Variable Camber Continuous Trailing Edge Flap (HLVCCTEF) Wing Configuration," *AIAA SciTech Forum*, No. 2015-1406, Kissimmee, FL, January 2015.

[12] Rodriguez, D. L., Aftosmis, M. J., Nemec, M., and Anderson, G. R., "Optimized Off-Design Performance of Flexible Wings with Continuous Trailing-Edge Flaps," *AIAA SciTech Forum*, No. 2015-1409, Kissimmee, FL, January 2015.

[13] Swei, S. S.-M., Zhu, G. G., and Nguyen, N. T., "LMI-based Multiobjective Optimization and Control of Flexible Aircraft Using VCCTEF," *AIAA SciTech Forum*, No. 2015-1844, Kissimmee, FL, January 2015.

[14] Ting, E., Dao, T., and Nguyen, N., "Aerodynamic Load Analysis of a Variable Camber Continuous Trailing Edge Flap System on a FlexibleWing Aircraft," *AIAA SciTech Forum*, No. 2015-1839, Kissimmee, FL, January 2015.

[15] Ting, E., Nguyen, N., and Lebofsky, S., "Static Aeroelastic Modeling of a Sub-ScaleWind Tunnel Model with Novel Flap Concept," *AIAA SciTech*, No. 2015-1407, Kissimmee, FL, January 2015.

[16] Chen, P. C., Zhou, Z., Ghoman, S. S., and Falkiewicz, N., "Low-Weight Low-Drag Truss-Braced Wing Design Using Variable Camber Continuous Trailing Edge Flaps," *AIAA SciTech Forum*, No. 2015-1176, Kissimmee, Florida, January 2015.

[17] Ferrier, Y., Nguyen, N., and Ting, E., "Real-Time Adaptive Least-Squares Drag Minimization for Performance Adaptive Aeroelastic Wing," *AIAA Aviation Forum*, No. 2016-3567, Washington, D.C., June 2016.

[18] Kaul, U. K. and Nguyen, N. T., "Lift Optimization Study of a Multi-Element Three-Segment Variable Camber Airfoil," *AIAA Aviation Forum*, No. 2016-3569, Washington, D.C., June 2016.

[19] Rodriguez, D. L., Aftosmis, M. J., Nemec, M., and Anderson, G. R., "Optimization of Flexible Wings with Distributed Flaps

at Off-Design Conditions," *Journal of Aircraft*, Vol. 53, No. 6, November-December 2016, pp. 1731–1745.

[20] Stanford, B. K., "Static and Dynamic Aeroelastic-Tailoring with Variable Camber Control," *15th AIAA Dynamics Specialists Conference*, No. 2016-1097, San Diego, CA, January 4-8 2016 2016.

[21] Stanford, B. K., "Static and Dynamic Aeroelastic Tailoring with Variable-Camber Control," *Journal of Guidance, Control, and Dynamics*, Vol. 39, No. 11, November 2016, pp. 2522–2534.

[22] Liu, Y. and Livne, E., "Robust Optimization of Variable-Camber Continuous Trailing-Edge Flap Static Aeroelatic Action," *AIAA Journal*, Vol. 55, No. 3, March 2017, pp. 1031–1043.

[23] Menon, A., Chakravarthy, A., Steck, J., and Nguyen, N., "Decentralized Optimal Adaptive Control Architectures for the VCCTEF Aircraft," *AIAA SciTech Forum*, No. 2017-1590, Grapevine, TX, January 2017.

[24] Ting, E.and Chaparro, D. and Nguyen, N.and Fujiwara, G. E. C., "Optimization of Variable-Camber Continuous Trailing-Edge Flap Configuration for Drag Reduction," *Journal of Aircraft*, 2018, article in advance.

[25] Rodriguez, D. L., Aftosmis, M. J., Nemec, M., and Anderson, G. R., "Optimization of Flexible Wings with Distributed Flaps at Off-Design Conditions," .

[26] Bartels, R. E., Scott, R. C., Allen, T. J., and Sexton, B. W., "Aeroelastic Analysis of SUGAR Truss-Braced Wing Wind-Tunnel Model Using FUN3D and a Nonlinear Structural Model," *AIAA SciTech Forum*, No. 2015-1174, AIAA, 2015.

[27] Nguyen, N., Ting, E., and Lebofsky, S., "Aeroelasticity of Axially Loaded Aerodynamic Structures for Truss-Braced Wing Aircraft," *AIAA SciTech Forum*, No. 2015-1840, 2015.

[28] Anderson, W. K. and Bonhaus, D. L., "An Implicit Upwind Algorithm for Computing Turbulent Flows on Unstructured Grids," *Computers and Fluids*, Vol. 23, No. 1, 1994, pp. 1–22.

[29] "FUN3D Manual," 2015.

[30] Spalart, P. R. and Allmaras, S. R., "One-Equation Turbulence Model for Aerodynamic Flows," *30th AIAA Aerospace Sciences Meeting and Exhibit*, No. 92-439, Reno, NV, January 6-9 1992.

[31] Silva, W. A., "AEROM: NASA's Unsteady Aerodynamic and Aeroelastic Reduced-Order Modeling Software," *Aerospace*, Vol. 5, No. 41, April 2018, pp. 1–18.

[32] Juang, J.-N. and Pappa, R. S., "An Eigensystem Realization Algorithm for Modal Parameter Identification and Model Reduction," *Journal of Guidance, Control, and Dynamics*, Vol. 8, 1985, pp. 620–627.

[33] Juang, J.-N., Phan, M., and Horta, L. G., "Identification of Observer/Kalman Filter Markov Parametrs: Theory and Experiments," *Journal of Guidance, Control, and Dynamics*, Vol. 16, 1993, pp. 320–329.

[34] Lewis, F. L., Vrabie, D., and Syrmos, V. L., *Optimal Control*, John Wiley and Sons, Inc., 2012, Chapter 8.